Improving the accuracy of catalyst pore size distributions from mercury porosimetry using mercury thermoporometry

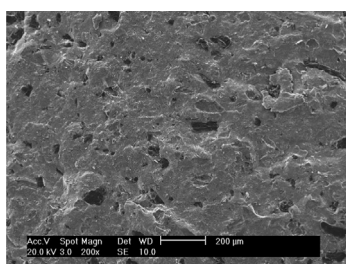Paul E. Dim [a], Rob S. Fletcher [b], Sean P. Rigby [a,*]

[a] Department of Chemical and Environmental Engineering, University of Nottingham, University Park, Nottingham NG7 2RD, U.K
[b] Johnson Matthey Process Technology Division, P.O. Box 1, Belasis Avenue, Billingham, Cleveland TS23 1LB, U.K

HIGHLIGHTS

- Resolution of controversy over impact of heavy metals.
- Demonstration of utility of complementary thermoporometry.
- Further use of integrated gas sorption in mercury porosimetry.
- Test of classification scheme for mercury porosimetry curves.

GRAPHICAL ABSTRACT

ABSTRACT

Mercury porosimetry is still frequently used to obtain the pore size distributions (PSDs) for porous heterogeneous catalyst pellets. However, unless the contact angle in the Washburn equation is correctly calibrated, porosimetry strictly remains only a relative technique. There is a particular potential issue for catalyst samples containing heavy metals, which may present (relatively) wetting surfaces to mercury, when the standard analysis is based upon the presumption of consistent non-wetting behaviour. Data in the literature on the impact of heavy metals on mercury intrusion is conflicting with some studies suggesting they do impact intrusion and some suggesting they do not. This study uses complementary gas sorption and mercury thermoporometry experiments that were fully serially-integrated with porosimetry to provide additional information to improve the interpretation of the basic mercury porosimetry data and validate the pore sizes obtained from it. These complementary data have been used to show that the wetting effect from heavy metals on intrusion may be confined to the smallest nanopores in the sample where the pore wall potentials begin to overlap. It has also been shown that confined mercury shows a significant advanced melting effect during thermoporometry. The thermoporometry studies revealed that the common interpretation of sharp intrusion curves and high entrapment levels in porosimetry data as implying ink-bottle pore geometries is flawed.

© 2015 Elsevier Ltd. All rights reserved.

1. Introduction

Mercury porosimetry remains a frequently used structural characterisation method for use with heterogeneous catalysts because it is still one of only a few techniques that can provide data over the complete length-scale range from ~3 nm to ~100 μm in a single experiment. A substantial body of past work on porosimetry has both greatly expanded its capabilities and revealed particular problems. For instance, there is much previous work in the literature on improving the interpretation of mercury porosimetry data and addressing key issues such as the pore-shielding effect (Androutsopoulos and Mann, 1979; Matthews et al., 1995). Mercury porosimetry relies upon the basic underlying principle that mercury is a non-wetting fluid for most surfaces and, thence, to intrude it into ever smaller pores a greater pressure is required, which according to the Washburn (1921)

---

equation is given by:

$$p_f^l = \frac{-2\gamma \, \cos \, \theta}{r} \qquad (1)$$

where p_f^l is the hydrostatic pressure in the liquid phase to enter a pore of radius r, γ is the surface tension, and θ is the contact angle. The macroscopic contact angle can readily be measured using techniques such as the sessile drop experiment. However, there is often doubt as to whether the macroscopic measurement applies to mercury menisci with a small radius of curvature, as would be found in nanopores. Previous workers have attempted to calibrate the physical properties term in the Washburn equation using model materials with independently known pore sizes, such as controlled pore glass (CPG) (Liabastre and Orr, 1978; Kloubek, 1981).

In the usual mercury porosimetry experiment, the hydrostatic pressure is increased in small steps, and the intruding mercury volume allowed to reach equilibrium at each step. The pore size is derived using Eq. (1), and the corresponding pore volume from the intruded liquid volume at each step. The accuracy of the pore size distribution relies upon Eq. (1), or its calibrated equivalents, being valid throughout the intrusion process, and, thence, that mercury always stays non-wetting to the surface. However, many of the catalysts used in the chemical industry use supported metal crystallites or mixed oxides of relatively heavy elements like copper, platinum and molybdenum. The dispersion force interaction of platinum is such that its Leonard–Jones potential parameters are the same as for mercury (Zhu, 1995). Hence, it is conceivable that the surface of catalysts containing heavy elements may wet mercury, contrary to the assumptions of the conventional analysis of mercury porosimetry data.

Mercury porosimetry is frequently used to obtain PSDs for catalyst pellets including those containing heavy metals, such as hydrotreating catalysts. However, since interpretation of mercury porosimetry is based upon the presumption that it is a non-wetting fluid, the presence of elements/surfaces for which it has a high affinity casts doubt over the accuracy of the PSDs obtained. Indeed, it has been found that increasing the content of MoO_3 or WO_3 in alumina-supported catalysts resulted in a gradual decrease in the apparent surface area from mercury intrusion porosimetry compared to that measured by the nitrogen adsorption BET method (Milbum et al., 1994). It was further found that altering the mercury contact angle towards a more wetting value improved agreement between the two methods. This suggested that the presence of heavy elements in the surface may alter the wetting properties of mercury and decrease the accuracy of the PSD. However, other workers Lowell and Shields (1982) found that the presence of other heavy elements, namely copper, nickel or cobalt, only increased the width of the hysteresis, and the amount of entrapment, but did not significantly alter the intrusion pressure. It could be argued that, since the pressure for mercury intrusion is controlled by the radius of curvature of the mercury meniscus at the pore mouth, then the presence of heavy elements down inside the pore will not impact intrusion pressure, but only retraction pressure due to the pore potential effect. Hence, uncertainty remains over the impact of heavy elements in the internal surface of a porous solid on the accuracy of the PSD obtained. The aforementioned contrasting findings could potentially be explained by the difference in atomic numbers of the elements studied, since molybdenum and tungsten are heavier elements, with larger dispersion forces, than copper, nickel or cobalt. However, even though both sets of workers studied alumina supports these differed in the pore size or surface roughness, and, thus, other characteristics of the system may explain the results. Lowell and Shields (1982) did not obtain independent validated measures of pore properties such as modal pore size to compare with mercury

intrusion. Hence, the particular influence of heavy metals on mercury intrusion remains an open question.

Recently, complementary methods have been developed that enable the more direct validation of mercury porosimetry. Following mercury intrusion the pressure is released in small steps to obtain a corresponding retraction curve as mercury extrudes from the sample. However, in many samples, not all of the mercury leaves the sample, and some may remain entrapped in the sample even when the pressure returns to ambient. The entrapped mercury remaining behind can itself be used as the probe fluid for thermoporometry. The mercury thermoporometry method (Bafarawa et al., 2014) enables the probing of the entrapped mercury directly to obtain information such as the size of the remaining mercury ganglia. Hence, mercury thermoporometry can be used to independently determine the size of pores that mercury has entered but then has become entrapped in the retraction step, and, thus, validate the mercury pore size obtained.

However, when using thermoporometry to probe complex pore geometries, the impact of that geometry on the melting mechanism and temperature has been shown to be important (Bafarawa et al., 2014). In particular, when the probe liquid ganglia extend between, and connect, several different pores, then so-called pore–pore interaction effects, such as advanced melting, become important (Hitchcock et al. 2011). In advanced melting, the melting of the fluid within a small pore connected directly to a larger pore can facilitate the melting of the probe fluid in the larger pore at a temperature lower than expected (for an isolated larger pore). Hence, in order to interpret (mercury) thermoporometry data correctly, the influence of pore and fluid ganglion connectivity, and network effects, needs to be taken into account, and will be considered in this study.

In order to use thermoporometry to validate porosimetry using entrapped mercury it is also necessary to fully understand the entrapment mechanism so that the correct interpretation of the thermoporometry data can be made. Typically, in thermoporometry, the porous solid is completely filled with probe fluid. While glass micro-model experiments (Wardlaw and McKellar, 1981) have shown that some particular pore geometries result in the pores being completely filled with mercury following entrapment, many other pore configurations only result in pores that are partially-filled with entrapped mercury. However, it has been shown previously (Rigby et al., 2006) that complementary integrated gas sorption experiments run on the same sample before and after mercury entrapment will reveal when the entrapment process leads to partial, rather, than full pore saturation with mercury. Hence, complementary integrated gas sorption will be used to resolve between different potential interpretations of the thermoporometry data.

Based on findings from mercury porosimetry experiments conducted on glass micro-models with simple created pore geometries (Wardlaw and McKellar, 1981) and other data, some authors (Day et al., 1994) have attempted to draw up a general classification scheme for the shapes of mercury porosimetry curves similar to the classification scheme developed by the IUPAC for nitrogen sorption isotherms and hysteresis loops (Rouquerol et al., 1999). However, there is doubt concerning the general applicability of these schemes to the wide variety of potential sample materials.

This work will show how the complementary measure of pore size provided by mercury thermoporometry can eliminate uncertainty over the accuracy of PSDs for catalysts containing heavy elements. In addition, this work will test the general applicability of the classification scheme for mercury porosimetry data, particularly the classical theory on the detection of ink-bottle pore geometry. The work comprises a detailed case study that makes use of the particular characteristics of the specific material chosen that make this type of study possible. Besides containing a

relevant heavy metal, namely copper, the entrapment level varies significantly with intrusion pressure and only really begins significantly after the intrusion curve has passed the point of inflection. This means that the modal pore size and beyond, should already have been filled on intrusion, for any entrapment level considered in the thermoporometry experiments. Hence, there was the potential (which was fulfilled) for entrapment to arise in the modal pore size for all partially entrapped samples considered.

2. Theory

2.1. Mercury porosimetry

In common usage, raw data from mercury porosimetry is processed using the Washburn (1921) equation. However, it is widely acknowledged (Kloubek, 1981) that both the surface tension γ and contact angle θ vary with the radius of curvature of the meniscus, and that the contact angle depends upon whether the meniscus is advancing or receding. More recently (Kloubek, 1981; Rigby, 2002) expressions for the term $\gamma.cos\,\theta$ have been developed that take into account these effects. These expressions have been obtained by calibrating the pressure p, at which mercury enters or leaves a model porous medium with a controlled structure, against a corresponding, independent measure of pore size r, such as electron microscopy (Liabastre and Orr, 1978). Insertion of these expressions into the Washburn equation gives rise to correlations of the form:

$$r = \frac{-A + \sqrt{A^2 - 2pB}}{p} \qquad (2)$$

where A and B are constants depending on the material, and whether the mercury meniscus is advancing or retreating. The values of A and B for silica and alumina are given in Table 1. The correlations of the form of Eq. (1) were determined using empirical methods, and are, therefore, of restricted range of applicability (see Table 1), and also contain experimental error ($\sim$4–5% (Kloubek, 1981). However, more recent work (Rigby and Chigada, 2010), using MF-DFT, has now shown that the calibrated Washburn equations remove apparent 'contact angle hysteresis' effects.

2.2. Thermoporometry

Thermoporometry is based upon the observation that, when a fluid is confined to a porous medium, the freezing and melting points of that fluid is changed. Typically, the shift in the phase transition point for a small crystal, relative to the bulk, varies inversely with crystal size (Mitchell et al., 2008). When a crystal is melting within a cylindrical pore the relevant form of the Gibbs–Thompson equation suggests the melting point depression ΔT_m will be given by:

$$\Delta T_m = T_m^\infty - T_m(x) = -\frac{4\sigma_{sl}T_m^\infty}{x\Delta H_f\rho_s}cos\,(\varphi), \qquad (3)$$

Table 1
Parameters for use in Eq. 2.

Material	$A.10^3$/(N m^{-1})	$B.10^{12}$/N	Range of validity/ (nm)
Silica (advancing meniscus)	− 302.533	− 0.739	6 − 99.75
Silica (retreating meniscus)	− 68.366	− 235.561	4 − 68.5
Alumina (advancing meniscus)	− 302.533	− 0.739	6 − 99.75
Alumina (retreating meniscus)	− 40	− 240	4 − 68.5

where $T_m(x)$ is the melting point in a pore of diameter x, T_m^∞ is the bulk melting temperature, ΔH_f is the bulk enthalpy of fusion, σ_{sl} is the surface tension, ρ_s is the density of the solid, and ϕ is the contact angle (typically assumed to be 180° for liquid–solid). This equation is often simplified to the form:

$$\Delta T_m = k/x, \qquad (4)$$

where k is the Gibbs–Thompson constant. In previous work (Bafarawa et al., 2014), it has been found that for melting of a mercury crystal via a hemispherical meniscus, the value of k is 90 nm K.

Borisov et al. (1998) found that a thin liquid layer forms on the surface of confined, solid mercury ganglia in the temperature range 195–229 K. This liquid-like layer forms the seed site for initiating melting of the solid cores at a higher temperature depending on characteristic size. It is presumed this liquid-like layer is one molecular diameter thick, and thus the effective crystal size in Eq. (4) becomes x–t, where t is the thickness of the liquid-like layer.

The differential pore size distribution can be obtained (Mitchell et al., 2008) from the equation:

$$\frac{dv}{dx} = \frac{k}{x^2}\frac{dv}{dT} \qquad (5)$$

where v is the volume of pores of size x.

For ice crystals that do not wet the solid there is generally a liquid-like layer that is always retained at the pore wall. It is from this existing molten phase layer that the melting process for the frozen phase is initiated. For a through ink bottle pore model, this process is shown in Fig. 1, where the arrows demonstrate how the liquid-like layer initiates the melting process and this melting mechanism is said to occur via sleeve-shaped menisci. When such a melting mechanism is in operation, the smaller necks will melt first, and, then, as the temperature is raised, the large pore will also subsequently melt. Therefore, this type of melting event would give an accurate measurement of the both the neck and body sizes.

However, for pores with a cylindrical geometry, melting could happen at a lower temperature via the alternative hemispherical meniscus (between solid and molten phases), than it would via a
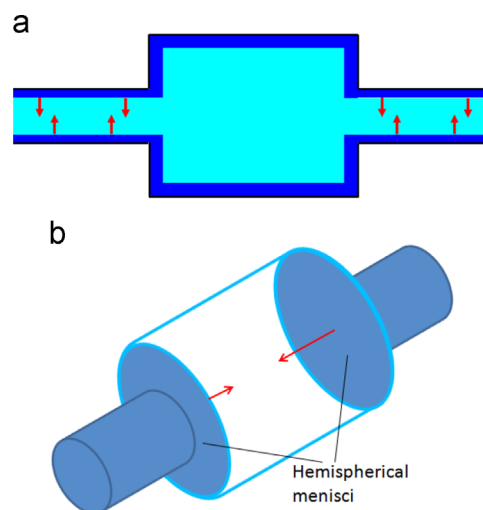

Fig. 1. Schematic depiction of the stages of the advanced melting process in a cylindrical, through ink-bottle pore system. The dark shading indicates the non-freezing surface liquid-like layer, while the light shading indicates the bulk frozen fluid. The arrows indicate the direction of the meniscus movement on initiation of melting from (a) sleeve-shaped menisci in the pore necks and (b) hemispherical menisci at the entrances to the pore body.

sleeve-shaped meniscus. For the through ink bottle pore in Fig. 1, melting would then be initiated within the outer narrow necks starting from the thin sleeve-shaped layer of permanently liquid-like fluid that exists at the pore wall. Once the fluid within these necks is fully molten, it will naturally produce a hemispherical meniscus at both ends of the larger pore body. These hemispherical menisci could then facilitate the melting of the solid in the large pore so long as the larger pore radius is smaller than the critical size for melting via a hemispherical meniscus at the current temperature. If that condition is met, then the larger pore would also melt at the same temperature as the smaller pore. Hence, the melting behaviour of the fluid confined within a void-space structure with two different, clearly-defined characteristic sizes, would make it erroneously appear as if the void space possessed just one size from the melting curve. Melting via a hemispherical meniscus might also be initiated from a dead-end pore, where the liquid-like layer covered the terminating wall.

3. Materials and methods

3.1. Materials

The material studied for the case study described in this work was a low temperature shift catalyst (ZnCu). It is a commercially available catalyst. Details of the catalyst composition and properties are presented in Table 2.

3.2. Methods

3.2.1. Mercury porosimetry

The experiments were carried out using a Micromeritics Autopore IV 9500, generally according to the method described in detail in Bafarawa et al. (2014) except where stated here. Prior to any experiment, the samples were oven dried at a temperature of 50 °C for 4 h. The equilibration times used in this work were 10, 15 and 30 s.

3.2.2. Gas sorption procedure

Nitrogen sorption experiments were performed using a Micromeritics Accelerated Surface Area and Porosimetry (ASAP) 2420 apparatus according to the method described in detail in Hitchcock et al. (2014) except where specified here. The amount adsorbed at different equilibration times was tested, and an appropriate equilibration time was found to be 10 s.

The gas adsorption data was analysed using the Barrett–Joyner–Halenda algorithm (Barrett et al., 1951), assuming a cylindrical sleeve meniscus geometry in the Kelvin equation, and using the Harkins–Jura t-layer correction equation, to obtain the pore size distribution weighted by pore volume. The adsorbate property factor was 0.953 nm.

3.2.3. Integrated gas sorption-mercury porosimetry-gas sorption procedure

The integrated gas sorption-mercury porosimetry-gas sorption procedure was performed according to the method described in detail in Hitchcock et al. (2014).

3.2.4. DSC-Thermoporometry

Mercury porosimetry was used to prepare the samples used in the thermporometry experiments. The DSC experiments were carried out using the apparatus, and generally according to the method, described in detail in Bafarawa et al. (2014) except where stated here. The sample with entrapped mercury was initially frozen in the DSC cell to the temperature of −80 °C, and then kept at this temperature for 30 min to ensure temperature homogeneity. The melting curves were measured over the temperature range from −80 °C to −37 °C at low scanning rate, 0.5 °C min^{-1}. Preliminary studies established this rate was the most appropriate. The DSC has the capability to measure heat flow rates with a resolution of ±0.5 μW and an accuracy of ±2 μW.

4. Results

Fig. 2 shows typical examples of the mercury porosimetry data for the ZnCu catalyst. From Fig. 2(a), it can be seen that different samples taken from the same batch of ZnCu catalyst have a range of values of total specific pore volume. However, the renormalized data in Fig. 2(b) indicates that the shapes of the intrusion curves are virtually the same for all samples. Hence, samples of the catalyst differ in the pore volume but not the pore size distribution. The standard deviation in the pore volume for the samples in Fig. 2(a) is ∼10% of the average. Fig. 2(c) also shows mercury intrusion scanning curves up to a range of different ultimate pressures, and the corresponding mercury retraction curves. The raw data have been adjusted to remove inter-particle intrusion effects. It can be seen that, while the shapes of the overlapping regions of the intrusion curves are quite similar, the amount of mercury entrapment depends strongly upon the ultimate intrusion pressure. The variation in mercury entrapment with intrusion pressure is much higher than the variation in total pore volume between samples, and thus entrapment level is dependent on ultimate intrusion pressure.

Fig. 3 shows the differential PSD obtained from the mercury intrusion curve up to an ultimate pressure of 414 MPa. The raw data have been analysed using Eq. (2) and the parameters for alumina given in Table 1. It can be seen that the modal peak occurs at a radius of ∼7–8 nm.

Fig. 4 shows the differential mercury ganglia size distributions obtained from DSC thermoporometry of the samples containing entrapped mercury following mercury porosimetry scanning curve experiments shown in Fig. 2(c). It can be seen that the shape of the ganglion size distribution following the 103 MPa scanning curve is bimodal with peaks at radii of ∼5–6 nm and ∼7–8 nm. It is also noted that the small size tail of the distribution extends below 5 nm down to a radius of ∼3 nm. However, it is noted that, according to Eq. (2), an intrusion pressure of 103 MPa corresponds to a pore radius of 5.9 nm. Hence, the data suggest that entrapped

Table 2
Composition and properties of catalyst studied.

Name	Principle components	Melting point/°C	Bulk density/kg m^{-3}	Length/mm	Diameter/mm	Form
Low temperature shift catalyst	Copper oxide Zinc oxide Aluminium oxide	>1400	1050	∼2.4	∼4.5	Tablet

Fig. 3. Differential pore size distribution determined from the mercury intrusion curve for the ZnCu catalyst analysed using Kloubek (1981) correlation (Eq. (2)).

Fig. 4. Differential pore size distributions, determined from the mercury thermoporometry melting curves and Eq. (5), for mercury entrapped after mercury intrusion up to ultimate pressures of 103 MPa, 110 MPa, 117 MPa and 414 MPa.

Fig. 2. Mercury intrusion curves for three whole pellet and one powder (particle size ∼100 μm) samples of the ZnCu catalyst with absolute cumulative intrusion volume (a), or fractional mercury saturation (b), against pressure (c), Mercury intrusion and retraction curves for whole pellet samples of ZnCu catalyst up to various ultimate intrusion pressures as indicated in legend. The raw data have been adjusted to remove inter-particle intrusion effects.

mercury ganglia exist with characteristic sizes less than the anticipated minimum penetrated pore radius for the ultimate pressure of the scanning curve. If the melting of the entrapped mercury ganglia was occurring via a cylindrical sleeve meniscus, and the appropriate Gibbs–Thompson parameter was then 45 K nm (Bafarawa et al., 2014), rather than a hemispherical meniscus, then the premature intrusion effect would be even more pronounced as the ganglia sizes would be shifted downwards in magnitude. From Fig. 4 it can also be seen that as the ultimate pressure of the porosimetry scanning curve is increased to intermediate pressures the size distribution of
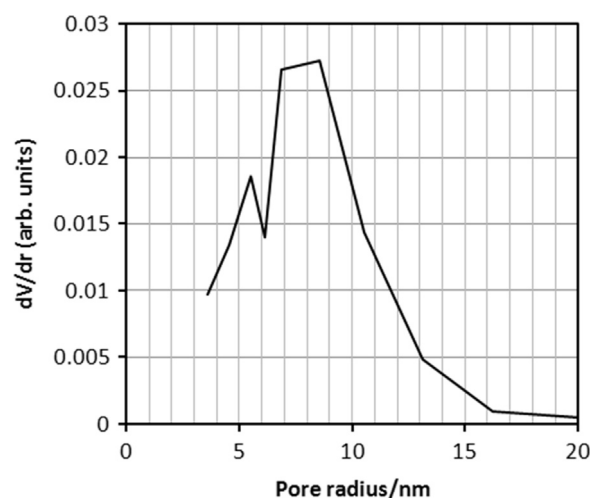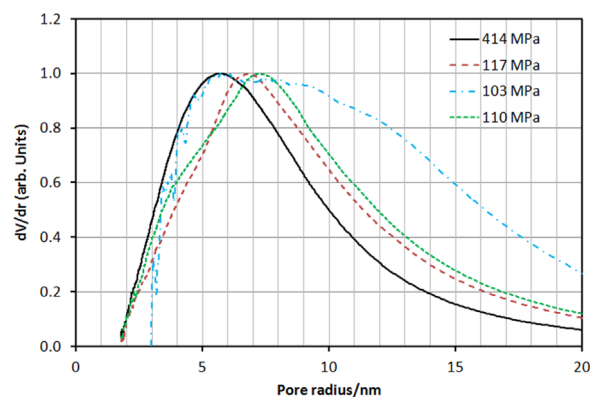
entrapped ganglia becomes narrower and more unimodal with the main peak at ∼7 nm. However, as the ultimate intrusion pressure is increased to the highest possible with the apparatus used (414 MPa), the modal peak position shifts down to ∼5–6 nm. It is also noted that the low size tail of the mercury ganglion size distributions progressively shifts to smaller sizes following scanning curves to ever higher ultimate intrusion pressures, as might be anticipated if mercury was intruding smaller pores with increasing pressure.

Fig. 5 shows nitrogen sorption isotherms obtained before and after mercury entrapment during porosimetry experiments with ultimate intrusion pressures of 414 MPa and 117 MPa. It can be seen that there is a significant reduction in total adsorbed nitrogen volume following porosimetry. The Gurvitsch volume for the nitrogen adsorption isotherms before porosimetry is typically 9% larger than the corresponding pore volume derived from mercury porosimetry for the same sample. While the gas adsorption isotherms show some tendency to level off at high pressures, they have not completely flattened out to a horizontal plateau, thereby indicating a small fraction of macropores may not have filled with condensed nitrogen at the top of the isotherm. However, the size of the Gurvitsch volume relative to the mercury pore volume suggests the volume of these macropores must be small. As explained in previous work (Hitchcock et al., 2015), for cylindrical pores open at both ends the Cohan equations suggest that the relative pressure for evaporation via a hemispherical meniscus is the square of the relative pressure required for condensation via a cylindrical sleeve meniscus. Also shown in Fig. 5 is a comparison
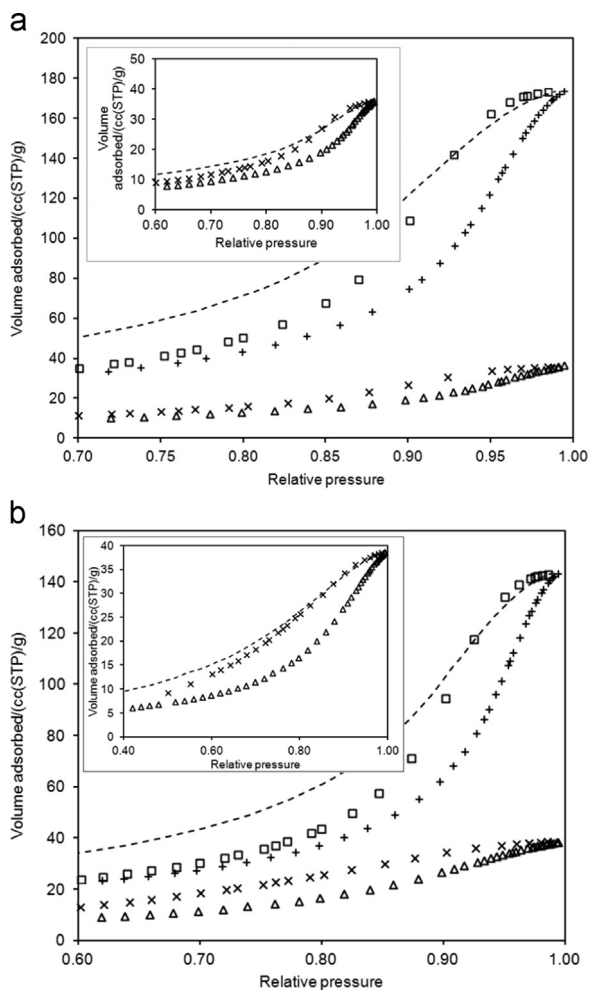
Fig. 5. Nitrogen sorption isotherms obtained before ($+$, adsorption; $\square$ desorption) and after ($\triangle$, adsorption; $\times$ desorption) mercury porosimetry to ultimate intrusion pressures of (a) 414 MPa and (b) 117 MPa. The dashed lines show the adsorption isotherms re-plotted after the original relative pressures have been squared. The inset shows an expanded view of the data after porosimetry.

of the experimental desorption isotherms measured with the prediction from the Cohan equations and the adsorption data. It can be seen that, in all cases (but particularly following mercury entrapment), the Cohan equations give a reasonably good prediction of the shape and position of the initial desorption knee at the top of the desorption isotherm. The agreement of the experimental desorption isotherm with the Cohan prediction declines with decreasing relative pressure.

Fig. 6 shows the difference in cumulative pore volume for the nitrogen adsorption pore size distributions obtained before and after a mercury porosimetry intrusion experiment to 414 MPa. It can be seen that, over the whole pore size range, the cumulative curve is always increasing, showing that more pore volume of a particular size is always lost, rather than generated, by mercury entrapment. Hence, the impact of mercury entrapment has been to reduce the accessible volume of pores of all sizes. The differential plot indicates that the modal pore radius of the pores in which mercury entrapment is occurring is $\sim$7 nm. The skew and modal peak position for the differential plot is similar to that for the mercury intrusion pore size distribution. The modal radius value is also similar to the modal peak position in the mercury thermoporometry pore size distributions following entrapment after intrusion to 110 or 117 MPa.
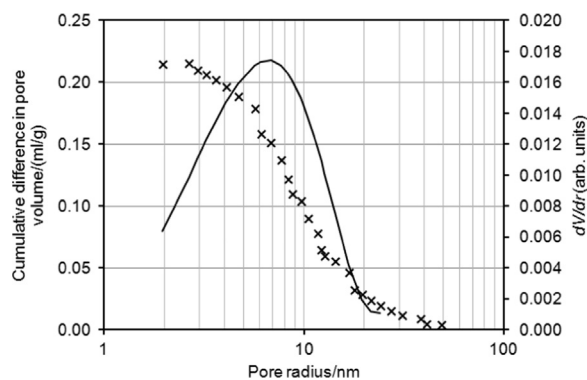

Fig. 6. Cumulative difference in pore volume ($\times$) for pore size distributions from before and after mercury intrusion to 414 MPa obtained from the integrated nitrogen adsorption experiments. Also shown (solid line) is the differential of the smoothed cumulative difference curve.

Fig. 7 shows secondary electron and back-scattered electron micrograph images of a wide field of a fracture surface of a sample of the ZnCu catalyst. It can be seen in the backscattered electron images that there are dark patches of low average molecular mass material surrounded by a 'sea' of higher average molecular mass material. These patches are probably graphite lubricant added to the pellet to aid tabletting. Fig. 8 shows two close-up views of a region of the surface of the catalyst where one of the black lumps of graphite has remained attached to the other, removed side of the cleavage surface, thereby revealing a cross-section of the catalyst. From Fig. 8, it can be seen that there are long narrow pore channels in the catalyst, together with wider pore inter-connections.

The images also show wispy and worm-like white features, for which the brighter white contrast indicates they have a relatively high average molecular mass. Due to the high molecular weight, relative to the rest of the material, and the nature of the sample, these features are probably copper metal with a thin passivated layer. These features, and the graphite lumps in Fig. 7, suggest that the surface of the catalyst, as seen by intruding mercury, is likely to be heterogeneous, including exposures of heavy metal, as well as intermediate mass oxide and alumina, and lower molecular mass graphite surfaces.

5. Discussion

The results from the integrated gas sorption and mercury porosimetry experiment suggest that pores that entrap mercury are completely filled with mercury. This is because, if partial filling of larger pores were occurring, it would be expected that the incremental volume of larger pores would decline, but that of smaller pores would increase, as small pores were apparently created. The small pores are apparently created from the gaps left free from mercury in the larger pores when filling is partial, as shown schematically in Fig. 9. The steeper cumulative pore size distribution at smaller sizes after porosimetry, compared to before, as shown in Fig. 9, would lead to one, or more, step(s) downwards in the cumulative difference plot in Fig. 6 with decreasing pore size. No data points with steps down at lower pore sizes were observed in Fig. 6, and, hence, the mechanism of entrapment for the catalyst sample seems to be complete pore-filling. Therefore it seems likely that the characteristic size of entrapped mercury ganglia detected in thermoporometry will correspond to the pore size in which they sit.

The ability of the Cohan equations to predict the position of the desorption knee in the nitrogen sorption data in Fig. 5 suggests
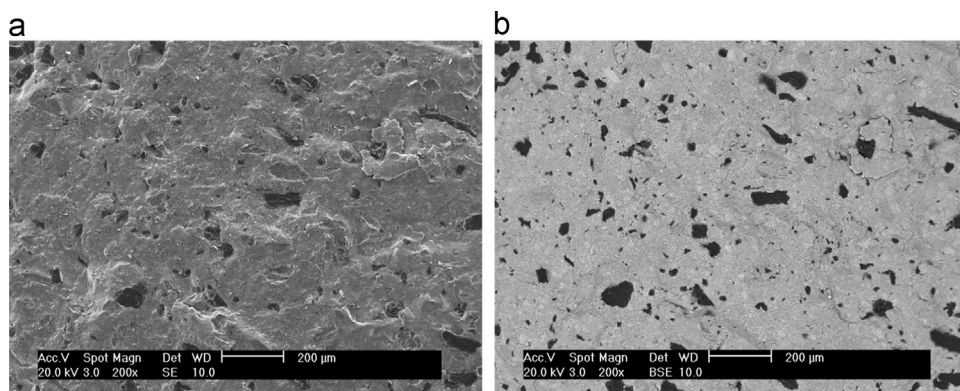
Fig. 7. Secondary electron (a) and back-scattered electron and (b) micrograph images of a wide field of a fracture surface of a sample of the ZnCu catalyst.
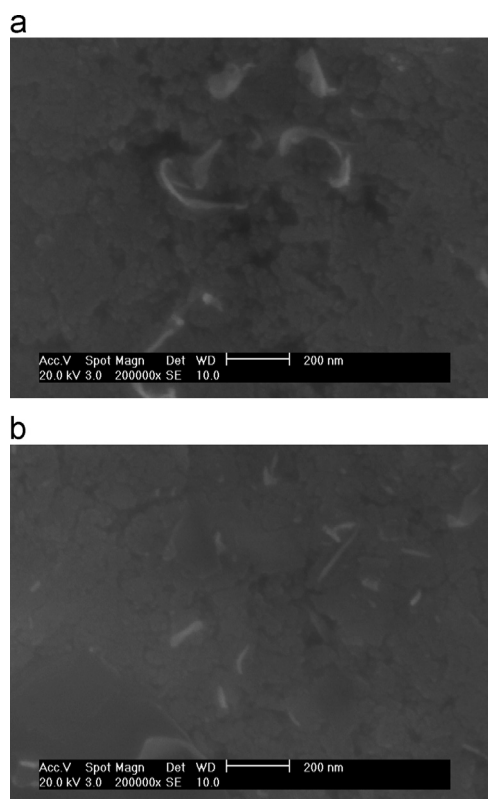

Fig. 8. Close-up SEM views of pore structure of ZnCu catalyst.

Fig. 9. BJH cumulative PSDs derived from nitrogen adsorption isotherms obtained before (solid line) and after (●) mercury porosimetry to 414 MPa on a hypothetical sample. The ultimate pore volume of the cumulative distribution obtained after porosimetry has been renormalised such that it is the same as that before porosimetry. The inset shows schematically how mercury entrapment causes loss of accessible pore volume and larger pores, and partial pore-filling leads to the apparent creation of smaller pores.

that a large fraction of pores are behaving like cylinders open at both ends, known as 'through' cylindrical pores. The narrowing of the gas sorption hysteresis at lower relative pressures is probably due to an increasing contribution from void-space regions in which nitrogen sorption is reversible, such as dead-end pores and surface roughness of larger pores. The similarity of the position of the mode of the differential pore size distribution obtained from nitrogen adsorption for pores that filled with mercury following intrusion to 414 MPa using the Cohan equation for a cylindrical sleeve meniscus, with the mode for the mercury intrusion suggests that the pores that entrap mercury are not suffering from significant pore-shielding effects. This would be consistent with them behaving like through cylindrical pores for gas sorption. In previous work (Hitchcock et al., 2014) it was shown that even uniform, straight cylindrical pores can entrap mercury if the menisci coalesce at the top of the intrusion curve such that the thread of mercury is continuous along the pore. In such circumstances mercury retraction can only commence by snap-off of the
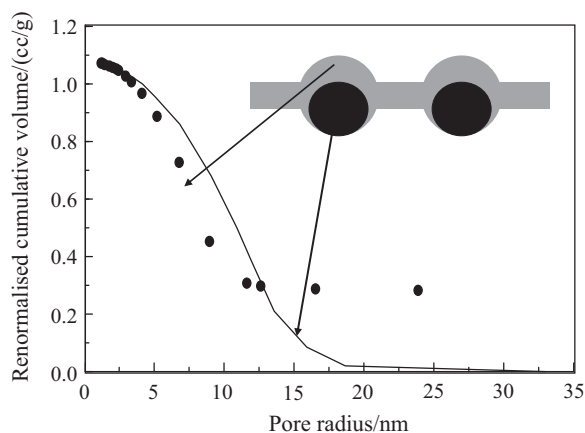
mercury thread to re-create two menisci. However, this snap-off process can occur at numerous sites along the length of a pore, where there is no mechanism to favour one site above all others (as does occur for ink-bottle pores with high neck-to-body size ratio), thereby creating several completely disconnected threads of mercury that thus become entrapped. The actual void space in the real material does not need to resemble a parallel pore bundle structure to lead to these results. Instead, it simply must lead to coalescence of menisci everywhere within pores of each size at the top of the mercury intrusion curve, and have no pore-shielding, such as might arise with the presence of macroscopic correlations in the spatial distribution of pore sizes.

From Fig. 4 it can be seen that when the levels of entrapped mercury are relatively low, for the lower ultimate pressure (110–117 MPa) intrusions in Fig. 2, the modal size of entrapped mercury ganglia is ∼7–8 nm, which is similar to the modal pore size in the distribution, obtained from the mercury intrusion curve analysed using the Kloubek (1981) correlations, shown in Fig. 3, and the differential nitrogen adsorption pore size distribution for pores entrapping mercury in Fig. 6. However, as the ultimate mercury intrusion pressure is increased, the amount of mercury entrapment increases and the apparent modal size of the entrapped ganglion distribution shifts to smaller sizes. These trends would be consistent with the onset and increasing pervasiveness of advanced melting effects in the thermoporometry data as mercury entrapment increases. This is because, as more mercury becomes entrapped, and the inter-connectivity of

residual mercury ganglia increases, more pathways are created to facilitate the advance of the melting front from small pores to neighbouring larger ones. This would cause a shift in the apparent size distribution, derived from thermoporometry, to smaller sizes. It is noted that even the lower pressure intrusion curves are still sufficiently high in pressure to intrude the modal pore size, and thus all can potentially give rise to entrapment within pores of the modal size from porosimetry. However, the presence of entrapped mercury in these modal pore sizes is then progressively obscured in the thermoporometry data as higher pressures enable smaller pores to also become filled and potentially entrap mercury, and thereby facilitate advanced melting in their neighbouring, filled, larger pores. Since smaller pores lying behind (but still connected to) larger pores can facilitate advanced melting, the presence of advanced melting is not inconsistent with the lack of shielding of modal sizes in the intrusion curve. The more disconnected and isolated nature of ganglia at low levels of mercury entrapment has meant that ganglia size distributions for lower entrapment levels are not impacted substantially by advanced melting effects. The similarity of the modal pore sizes obtained from mercury intrusion and thermoporometry for low and intermediate levels of entrapment suggests there is no shielding effect of the modal pore size by smaller pores for intrusion.

If there is no significant shielding of a large proportion of the pore size distribution then the mercury entrapment observed must have another cause other than ink-bottle type network geometry. In Fig. 2, the level of mercury entrapment increases with increased ultimate intrusion volume, with a particular marked increase in entrapment levels between scanning curves to ultimate pressures of 103 MPa and 117 MPa despite the ultimate intrusion volume only varying slightly. This step increase in entrapment with intruded volume might be associated with the last pores being intruded that were required to achieve final completion of a continuous thread of mercury at the top of the intrusion curve, rather than leaving significant free menisci to initiate retraction without the need for snap-off. In Fig. 2, there is a shift in the position of the knee, at the start of significant levels of retraction of mercury, to lower extrusion pressures with increased ultimate intrusion pressure, leading to a general widening of the hysteresis with increased intrusion pressure. This may the result of the need to lower pressure more substantially to initiate snap-off before retraction can begin, rather than it able to commence earlier from pre-existing, free menisci.

The similarity of the thermoporometry modal ganglion size (for mercury entrapped following scanning curves to 117 MPa) and the modal pore size from mercury intrusion suggests that for relatively larger mesopores of sizes greater than ~6 nm the mercury intrusion pressure is not influenced by any enhanced wetting properties of the wall. However, the appearance of mercury ganglia of sizes smaller than the size of pores predicted to be intruded by the Kloubek correlation, when the entrapment mechanism involves complete pore-filling, suggests that for the smallest pores there is an enhanced wetting effect leading to 'premature' intrusion. With other materials, such as CPGs and sol–gel silicas (Rigby and Edler, 2002), the Kloubek correlations have been shown to be correct down to the smallest mesopore sizes accessible with porosimetry. Kloubek (1981) suggested some time ago that there was a metastable structuring of molecules in the interfacial region (mercury/solid/air) due to the force field of the solid and bulk liquid that affects the local liquid density, and is responsible for the contact angle hysteresis in porosimetry because of a gradient in local liquid density depending on whether it has just passed over a more, or less, wetting surface. It also seems likely that this influence of surface heterogeneity on liquid density affecting contact angle would be more significant in smaller pores where the aforementioned force field of the solid is stronger closer to the centre of the pore. Hence, it is suggested that this is probably the mechanism by which the presence of heavy metals does affect the accuracy of porosimetry in small pores.

6. Conclusions

It has been shown that rather than particular mercury porosimetry data of the form of a sharp intrusion curve followed by high entrapment on retraction being associated with ink-bottle pores, in this case there was very little shielding of the pore size distribution and the high entrapment was thus probably due to mercury stabilisation due to high pore interconnectivity. This suggests that common interpretations and classification schemes for mercury porosimetry curves should be treated with caution. It has also been shown that advanced melting effects arise in thermoporometry using mercury as the probe fluid. The data presented here suggested that mercury intruded smaller pores in the ZnCu catalyst at lower pressures than might have been anticipated given its behaviour in larger pores. This has been attributed to the greater overlap of pore wall potentials in narrow pores with walls containing elements with strong dispersion interactions.

References

Androutsopoulos, G.P., Mann, R., 1979. Evaluation of mercury porosimetry experiments using a network pore structural model. Chem. Eng. Sci. 34, 1203–1212.

Bafarawa, B., Nepryahin, A., Ji, L., Holt, E.M., Wang, J., Rigby, S.P., 2014. Combining mercury thermoporometry with integrated gas sorption and mercury porosimetry to improve accuracy of pore-size distributions for disordered solids. J. Coll. Interface Sci. 426, 72–79.

Barrett, E.P., Joyner, L.G., Halenda, P.H., 1951. The determination of pore volume and area distributions in porous substances-I. Computations from nitrogen isotherms. J. Am. Chem. Soc. 73, 373–380.

Borisov, B.F., Charnaya, E.V., Plotnikov, P.G., Hoffmann, W.D., Michel, D., Kumzerov, Y.A., Tien, C., Wur, C.S., 1998. Solidification and melting of mercury in a porous glass as studied by NMR and acoustic techniques. Phys. Rev. B 58, 5329–5335.

Day, M., Parker, I.B., Bell, J., Fletcher, R., Duffie, J., Sing, K.S.W., Nicholson, D., 1994. Modelling of mercury intrusion and extrusion. Stud. Surf. Sci. Catal. 87, 225–234.

Hitchcock, I., Holt, E.M., Lowe, J.P., Rigby, S.P., 2011. Studies of freezing-melting hysteresis in cryoporometry scanning loop experiments using NMR diffusometry and relaxometry. Chem. Eng. Sci. 66, 582–592.

Hitchcock, I., Lunel, M., Bakalis, S., Fletcher, R.S., Holt, E.M., Rigby, S.P., 2014. Improving sensitivity and accuracy of pore structural characterisation using scanning curves in integrated gas sorption and mercury porosimetry experiments. J. Coll. Interface Sci. 417, 88–99.

Kloubek, J., 1981. Hysteresis in porosimetry. Powder Technol. 29, 63–73.

Liabastre, A.A., Orr, C., 1978. Evaluation of pore structure by mercury penetration. J. Coll. Interface Sci. 64, 1–18.

Lowell, S., Shields, J.E., 1982. Influence of pore potential on hysteresis and entrapment in mercury porosimetry. J. Coll. Interface Sci. 90, 203–211.

Matthews, G.P., Ridgway, C.J., Spearing, M.C., 1995. Void space modelling of mercury intrusion hysteresis in sandstone, paper coating and other porous media. J. Coll. Interface Sci. 171, 8–27.

Milbum, D.R., Adkins, B.D., Davis, B.H., 1994. Alumina supported molybdenum and tungsten oxide catalysts. Surface area and pore size distribution from nitrogen adsorption and mercury penetration. Appl. Catal. 119, 205–222.

Mitchell, J., Webber, J.B.W., Strange, J., 2008. Nuclear magnetic resonance cryoporometry. Phys. Rep. 461, 1–36.

Rigby, S.P., 2002. New methodologies in mercury porosimetry. Stud. Surf. Sci. 144, 185–192.

Rigby, S.P., Chigada, P.I., 2010. MF-DFT and experimental investigations of the origins of hysteresis in mercury porosimetry of silica materials. Langmuir 26, 241–248.

Rigby, S.P., Edler, K.J., 2002. The influence of mercury contact angle, surface tension and retraction mechanism on the interpretation of mercury porosimetry data. J. Coll. Interface Sci. 250, 175–190.

Rigby, S.P., Evbuomwan, I.O., Watt-Smith, M.J., Edler, K.J., Fletcher, R.S., 2006. Using nano-cast model porous media and integrated gas sorption to improve fundamental understanding and data interpretation in mercury porosimetry. Part. Part. Syst. Charact. 23, 82–93.

Rouquerol, F., Rouquerol, J., Sing, K., 1999. Adsorption by Powders and Porous Solids: Principles, Methodology and Applications. Academic Press, London.

Wardlaw, N.C., McKellar, M., 1981. Mercury porosimetry and the interpretation of pore geometry in sedimentary rocks and artificial models. Powder Technol. 29, 127–143.

Washburn, E.W., 1921. The dynamics of capillary flow. Phys. Rev. 17, 273–283.

Zhu, S.-B., 1995. Interaction of water, ions and atoms with metal surfaces. Surf. Sci. 1995 (329), 276–284.